Temperature-driven nutrient recycling and euxinia as a marine mass extinction mechanism

Dominik Hülse,[1] Kimberly V. Lau,[2,3] Sebastiaan J. van de Velde,[1]
Sandra Arndt,[4] Katja M. Meyer,[5] Andy Ridgwell[1]

[1] *Department of Earth and Planetary Sciences, University of California, Riverside, CA, USA*

[2] *Geosciences and Earth and Environmental Systems Institute, The Pennsylvania State University, University Park, PA ,USA*

[3] *Geology and Geophysics, University of Wyoming, WY, USA*

[4] *Bgeosys, Geoscience, Environment & Society, Université Libre de Bruxelles, Brussels, Belgium*

[5] *Environmental Science, Willamette University, Salem, OR, USA*

Extreme warming at the end-Permian induced profound changes in marine biogeochemical cycling and animal habitability, leading to the largest extinction in Earth's history. However, a causal mechanism for the extinction that explains the various proxy evidence has yet to be determined. By combining recent modeling developments with global and local redox observations, we show, in an Earth system model, that a temperature-driven increase in microbial respiration can reconcile reconstructions of the spatial distribution of euxinia and seafloor anoxia spanning the Permian/Triassic transition. We illustrate how enhanced metabolic rates would have strengthened upper ocean nutrient (phosphate) recycling, and thus shoaled and intensified the oxygen minimum zones, eventually causing euxinic waters to expand onto continental shelves and poison benthic habitats. Enhanced microbial activity in

the ocean interior also lowers subsurface dissolved inorganic carbon isotopic values with the implication that carbon release as inferred from observed isotope changes is likely overestimated. Our findings present a novel view of the sensitive interconnections between temperature, microbial metabolism, ocean redox state and carbon cycling during the end-Permian mass extinction with potential far-ranging implications for the interpretation of carbon cycle perturbations during Earth history.

Climate warming driven by volcanic greenhouse gas release is widely regarded as the underlying driver for the largest metazoan extinction event in Earth's history at the end of the Permian Period when $\sim$80% of marine species were eliminated[1–4]. Proxy evidence, spanning the Permian/Triassic transition (P/Tr, 251.9 Ma[5]), reveals a 7-10°C increase in sea surface temperature occurring in as little as $\sim$39 kyr[6–8] (Fig. 1a+d), the development of (photic-zone) euxinia (waters containing sulphide[9]), an expansion in the extent of seafloor anoxia[10,11], and a decrease in the carbon isotopic signature recorded in carbonates[12] (δ^{13}C, Fig. 1e). Although the extinction event itself has been intensely studied and is relatively well characterized, the mechanisms behind the development of widespread de-oxygenation and biodiversity loss are still not fully understood [13].

Proposed explanations linking these observations with the extinction all require reduced oxygenation of the ocean, but fundamentally diverge in the cause of this change. In particular, previous 3D Earth system model (ESM) studies have required either a sustained collapse of global ocean circulation in conjunction with a much weaker biological pump[14], or a well ventilated end-Permian ocean with a much stronger biological pump driven by enhanced nutrient (generally phosphate) availability[15,16]. Other modelling work[17] has demonstrated that increasing the ocean phosphate inventory can account for widespread subsurface euxinia, but this not only requires an excessive increase in phosphate availability but also causes near-global anoxia in the deep sea[18], which is in conflict with paleoredox estimates from uranium isotope records[11,19] (Fig. 1b+c). Further explanations have focused on reducing oxygen availability throughout the ocean as a whole, either through the oxidation of methane released from hydrates[15] or of a massive reservoir of dissolved organic matter[20], or via warming driven by the CO_2 release associated with volcanism[21,22]. As carbon release mechanisms, these processes can also account for an observed pronounced decline in ocean carbon $\delta^{13}C$[12]. Finally, some studies [23–25] hint that a change in the gradient in $\delta^{13}C$ between surface and subsurface might have occurred. If correct, this might be explained by ecologically-driven changes in organic matter sinking rates or reactivity [25–27] that drive a vertical repartitioning of organic carbon respiration (and hence $\delta^{13}C$) in the ocean, although the nature and impact of such changes remain to be quantified. Here, by recognizing the universally important role of temperature in controlling microbial respiration[28], we provide a simple mechanistic and data-constrained explanation for how expanded oxygen-minimum zones[26,27] and (episodic) shoaling of sulfidic waters[29] could have occurred and hence acted as an important kill mechanism during the mass extinction.

Oxygen availability in the water column generally decreases from well-mixed surface waters (few tens of meters), to the oxygen minimum zone (OMZ, typically at a depth of a few hundreds of meters). Along with ocean circulation, this gradient is controlled by the remineralization of particulate organic matter (POM) which consumes oxygen and releases inorganic nutrients (and carbon), that can be returned by mixing, upwelling and diffusion back to the surface to fuel new primary productivity[30]. Critical here is the sinking rate and reactivity of POM, as it controls where in the water column and how quickly this remineralization occurs, and thus, the depth and intensity of OMZs[18,31]. We posit that a further factor, and the key to understanding how the marine environment changed across the P/Tr, is ocean temperature[28,32].

A mechanistic representation of the biological pump

To demonstrate the importance of a warming ocean in driving subsurface euxinia and potentially widespread extinction across shallow marine environments, we simulate spatial redox distributions for a range of P/Tr conditions using the cGENIE ESM[33,34]. We modify the widely used "static" representation of the biological pump (i.e. an invariant POM remineralization depth profile[35]) to explicitly account for the impact of ocean warming at the end-Permian on remineralization (SI). In addition, we decrease the sinking rate of POM in the model by $\sim$22% – scaled to the smaller mean animal biovolume at the end-Permian ([36], SI) – to reflect the shallower remineralization profile inferred prior to the rise of pelagic calcifiers in the early Mesozoic[31]. Finally, we account for progressive changes in the susceptibility of POM to microbial remineralization as it reacts with sulphide (H_2S) in the water column (SI), in a process known as "sulfurization"[37]. Because the time-scale of warming leading up to the P/Tr boundary is slow relative to the adjustment time-scale of large-scale ocean circulation (i.e. warming likely occurred over $\sim$39 kyr or more, starting in the *C. meishanensis* biostratigraphic zone[5,8]), a series of (10 kyr) steady-state simulations can be used to approximate the biogeochemical response to a sequence of warming stages. In these, we prescribe a range of atmospheric $p\text{CO}_2$ values (1 – 30 × pre-industrial $p\text{CO}_2$, i.e. 280–8400 ppmv), chosen to span the increase in tropical Tethys ocean temperatures reconstructed from proxy records (from about 22 to 35°C, Fig. 1a+d, SI). Simultaneously, we explore the importance of varying the ocean phosphate inventory (1 – 2.5× modern) to represent the potential net impact of increased weathering and sediment regeneration rates as the climate warmed and ocean anoxia increased, respectively[38–40]. We thereby create a gridded model parameter ensemble of varying climate vs. ocean nutrient state. To simplify the analysis of the impacts of temperature-dependent remineralization, we do not address in this study the question of which nutrient actually limited primary production during the P/Tr. Rather, we vary the dissolved phosphate inventory simply as a means of generating different states of global export and anoxia that can be tested against observations. Atmospheric oxygen is fixed at modern levels but our main findings are independent of this assumption (SI).

Constraining model results with global and local redox proxies

Uranium isotopes can provide powerful constraints on ocean models via the reconstructed extent of seafloor anoxia (f_{anox}) . To quantitatively compare the ESM results with a compilation of carbonate δ^{238}U data over the P/Tr transition (SI), we use a forward box model that encapsulates the uncertainties in the U isotope budget (adapted from Lau et *al.*[11]). According to our U-model results, the δ^{238}U data can be best explained by an abrupt increase in f_{anox} that either coincided with the EH, or preceded it by much less than the onset of the warming event (Fig. 1 b+c). An increase of f_{anox} from a modern value of 0.6% to at least 30% (i.e. a factor of more than 50) represents our preferred minimum scenario as smaller perturbations fail to simulate the rate of change and magnitude of the shift in the δ^{238}U data (Extended Data Fig. 4).

We also ground-truth the ESM results with a new compilation of local redox proxies (Extended Data Fig. 1 and Extended Data Table 2). The dataset consists of geochemical, lithologic, sedimentologic, and biomarker evidence for water-column euxinia and bottom water anoxia and distinguishes three phases of the P/Tr transition (Late Permian background, Pre-Extinction Horizon and Main Extinction, Extended Data Table 2; see SI for definitions). The Late Permian data only indicate photic-zone euxinia occurring at the Meishan section with no clear evidence for seafloor anoxia (Fig. 3a+g, Extended Data Table 2). Immediately before the EH, water-column euxinia expanded to sections in British Columbia (BC), Shangsi, and potentially to the equatorial Panthalassic (Japan), while unequivocal evidence for bottom water anoxia remains limited and only exists for BC (Fig. 3b+h). In contrast, during the Main Extinction, anoxia spread across much of the shallow seafloor, and multiple lines of evidence suggest widespread euxinia impinged on shallow marine habitats (Fig. 3c+i).

Impact of temperature-driven respiration on the marine redox-landscape

Our model experiments show that for a "static" (fixed remineralization profile) biological pump, global POM cycling (i.e. POM export production, rain and burial rates within the sediment) is almost entirely controlled by nutrient (here, PO_4) availability, with a minor increase at higher temperatures attributable to temperature-dependent productivity (Fig. 2a–c). Global mean photic-zone $[H_2S]$ shows little temperature sensitivity and remains below $4\mu\text{mol kg}^{-1}$ (Fig. 2d) and the depth of maximum $[H_2S]$ is generally below 400m (Extended Data Fig. 8). At the same time, the extent of seafloor anoxia increases to values above 30% even at moderately high warming and/or phosphate increases (Fig. 2e). The relative lack of sensitivity of shallow euxinia vs. deep anoxia cannot easily be reconciled with observations for photic-zone euxinia (Extended Data Fig. 8) and expanded seafloor anoxia (Fig. 1b+c), respectively.

In contrast, the assumption of a temperature-dependent biological pump results in progressively more phosphate being released shallower in the water column with warming. Shifting the depth of regenerated phosphate closer to the ocean surface means that diffusive transport together with ocean mixing and upwelling processes (which we find are largely independent of warming at steady state, SI) drive an increased re-supply flux of phosphate back to the photic zone, enhancing export production (Fig. 2f, and Extended Data Fig. 5a–d). Although POM export production increases by up to a factor of three with warming compared to the static model, the POM rain to the sediments does not change significantly (Fig. 2g), due to a greater proportion of remineralization and recycling taking place higher up in the water column. This positive nutrient recycling feedback is further intensified by the assumed slower-than-modern sinking rate in the Paleozoic[31] (Extended Data Fig. 5c), as it increases the residence time of POM in the upper ocean, leading to more complete remineralization and phosphate recycling. Mean photic-zone [H_2S] is substantially higher (reaching values $> 60\mu$mol kg^{-1}) and highly sensitive to temperature variations (Fig. 2i). Notably, higher temperatures cause an increase in upper ocean [H_2S] and a concomitant shoaling of the chemocline – even without the need to invoke any change in phosphate inventory (Extended Data Fig. 9). In addition, increased ocean euxinia leads to higher sulfurization rates causing POM burial rates to increase (Fig. 2h) and the extent of seafloor anoxia to decrease (compare Fig. 2j+e), a negative feedback that may be important in the transition back to a more oxygenated ocean[41].

At least at the relatively coarse grid resolution (10° in longitude, variable $3-19°$ in latitude) employed in cGENIE, our model predictions for the spatial distribution of euxinia and seafloor anoxia appear in general agreement with the available evidence for local redox-conditions (Fig. 3, see SI for more details) and our U-model results (Fig. 1b+c). In our "Late Permian background" scenario (i.e. lower temperatures and modern ocean [PO_4]), only a few very local environments developed [H_2S] around 20–30μmol/kg and are limited to depths below 284m (Fig. 3a+d), similar to profiles in the modern Cariaco Basin[42]. Instances of upper ocean euxinia were very limited in spatial extent and only occurred in the Eastern Equatorial Panthalassic and the Eastern Tethys (South China). The simulated extent of bottom water anoxia, 0.7% of the seafloor, is comparable to the modern value of 0.6% ([43], Fig. 3g). Consistent with proxy reconstructions, climate warming together with a moderate release of phosphate (i.e. the "Pre-Extinction Horizon" phase), resulted in increasing [H_2S], with sulphidic waters impinging onto continental shelves and slopes, especially in warm equatorial waters (Fig. 3b+e). While most of the global seafloor remains oxic ($f_{anox} = 1.7\%$), approximately 20% of the seafloor shallower than 1000m exhibits [O_2] <60μmol/kg (Fig. 3h, Extended Data Table 4), a typical threshold for hypoxic conditions and considered critical for the survival of many modern marine animals[30]. A second increase in temperature, together with another slight relaxation of phosphate-limitation (i.e. a $\sim$7°C warming of SSTs and a doubling of ocean [PO_4] compared to modern) is sufficient to simulate the "Main Extinction". This scenario satisfies not only local evidence for an expansion of upper ocean euxinia (Fig. 3c) but also predicts more widespread seafloor anoxia that has spread to the abyssal plain (Fig. 3i), in broad agreement with inferences from δ^{238}U data (Fig. 1b+c). The habitable area in the upper ocean is further restricted as now $\sim$30% of the seafloor above 1000m exhibits hypoxic conditions (Extended Data Table 4).

Implications for ocean redox and carbon cycle dynamics

Given the relatively prolonged interval of warming in the lead up to the P/Tr boundary ($\sim$39 kyr[8]), our analysis favors a conceptual model in which higher metabolic rates drive a pronounced vertical partitioning in ocean redox. This biologically driven partitioning occurs within an ocean that remains not only well ventilated at depth (Extended Data Fig. 10) but is characterized by a slightly greater overturning strength at warmer states (Figure 3j-l). Although this behavior is consistent with previous steady-state modelling results[15,44], we note that our model utilizes a fixed wind field as a boundary condition and hence does not account for (more regional) ocean circulation impacts of changing atmospheric dynamics with warming. Furthermore, while we find that the temperature impact on metabolic rates is sufficient to provide an effective kill mechanism for the upper ocean ecosystem, pelagic ecosystem changes associated with the extinction itself, which we do not account for in our modeling, could also have played a role in driving a further vertical re-partitioning of oxygen consumption, such as through further changes in organic matter sinking rates or its reactivity [25–27]. Finally, we recognize that we do not account for limitation of productivity by nutrients other than phosphate. However, previous dual nutrient (N+P) modeling work has found that despite increasing rates of denitrification in a more anoxic ocean, export production still responds approximately linearly to changes in phosphate inventory, with production increasingly supported by ammonium assimilation and nitrogen fixation in place of nitrate assimilation [45]. The role of iron in the P/Tr ocean is much more uncertain, and could provide either a positive feedback on productivity through increased solubilization (as Fe^{2+}) and bioavailability, or a negative feedback when combined with sulphide in the water column and removed as pyrite (Fe_2S), and remains a general unknown in ocean circulation model studies of deep time.

Irrespective of the simplified nutrient dynamics, our new temperature and biological pump centric model is in contrast with strong physical partitioning such as simulated by Penn et *al.*[14] using the Community Earth System Model (CESM), where instantaneous warming drives persistent (multi kyr) stratification of the ocean. These two conceptual (and numerical) models also fundamentally differ in the consequent predictions of biological export – more vigorous overturning circulation, in conjunction with temperature-driven phosphate recycling substantially enhances export here, whereas stratification severely restricts upwelling and hence export in CESM – with important implications for the stressors associated with the marine extinction. Given that the initial ocean circulation response of the cGENIE ESM to instantaneous warming is very similar to that of CESM immediately after the perturbation (Extended Data Fig. 12), it is the assumed time-scales of warming that fundamentally distinguish between these states, highlighting the importance of refined age models and temperature reconstructions for the P/Tr.

Our inference of a metabolically driven (rather than transient circulation-driven) redox partitioning allows for persistently high temperatures during the Early Triassic[6] to prolong the occurrence of extensive seafloor anoxia[11]. Low levels of atmospheric O_2[46] together with episodic volcanism in the Early Triassic[47] and consequent oscillations between sulfidic and oxic conditions potentially played a role in the protracted biogeochemical and biological recovery prior to the

Middle Triassic. There may also be implications for changes in particle sinking speed that are potentially associated with the advent of pelagic biomineralization in the early Mesozoic Marine Revolution[31,48], with our results indicating that a given warming perturbation will drive a larger absolute increase in POM export during the Paleozoic when sinking rates are slower.

Finally, our numerical model analysis sheds new light on the δ^{13}C decline itself, and specifically the cause for substantive variability in what is nominally a globally imprinted signal. Differences in onset timing, temporal evolution, and maximum isotopic change of the end-Permian δ^{13}C negative shift have been observed among stratigraphic sections[12] (e.g. the amplitude varies between 4 and 7‰), complicating estimates of the size and source of the carbon cycle perturbation. We simulate a maximum decrease in the Tethys Ocean subsurface δ^{13}C during the P/Tr of 3.9‰ – approximately 60% of the observed δ^{13}C decrease in Armenia and Iran, with a smaller shift occurring in colder waters (Fig. 1e). This decline is driven only by temperature-induced changes to the biological pump in the model without invoking changes in the ocean+atmosphere carbon inventory (see SI). The implication is that end-Permian carbon release, as inferred from observed δ^{13}C changes (e.g. Erwin[13]), is likely overestimated, with the total release being smaller and/or the isotopic composition of the source is less negative, than previously assumed. This implies that carbon from volcanism rather than a reduced source (e.g. organic matter) was more dominant. In sum, these results not only reassess the relationship between temperature and the ocean redox state but also carbon cycle perturbations recorded by δ^{13}C.

1. Erwin, D. H. The PermoTriassic extinction. *Nature* **367**, 231–236 (1994).
2. Renne, P. R., Black, M. T., Zichao, Z., Richards, M. A. & Basu, A. R. Synchrony and Causal Relations Between Permian-Triassic Boundary Crises and Siberian Flood Volcanism. *Science* **269**, 1413–1416 (1995).
3. Stanley, S. M. Estimates of the magnitudes of major marine mass extinctions in earth history. *Proceedings of the National Academy of Sciences* **113**, E6325–E6334 (2016).
4. Burgess, S. D., Muirhead, J. D. & Bowring, S. A. Initial pulse of Siberian Traps sills as the trigger of the end-Permian mass extinction. *Nature Communications* **8**, 1–6 (2017).
5. Burgess, S. D., Bowring, S. & Shen, S.-z. High-precision timeline for Earths most severe extinction. *Proc. Natl. Acad. Sci. U.S.A.* **111**, 3316–3321 (2014).
6. Sun, Y. *et al.* Lethally Hot Temperatures During the Early Triassic Greenhouse. *Science* **338**, 366–370 (2012).
7. Joachimski, M. M. *et al.* Climate warming in the latest Permian and the PermianTriassic mass extinction. *Geology* **40**, 195–198 (2012).
8. Joachimski, M. M., Alekseev, A. S., Grigoryan, A. & Gatovsky, Y. A. Siberian Trap volcanism, global warming and the Permian-Triassic mass extinction: New insights from Armenian Permian-Triassic sections. *GSA Bulletin* **132**, 427–443 (2020).
9. Grice, K. *et al.* Photic Zone Euxinia During the Permian-Triassic Superanoxic Event. *Science* **307**, 706–709 (2005).

10. Brennecka, G. A., Herrmann, A. D., Algeo, T. J. & Anbar, A. D. Rapid expansion of oceanic anoxia immediately before the end-Permian mass extinction. *Proc. Natl. Acad. Sci. U.S.A.* **108**, 17631–17634 (2011).

11. Lau, K. V. *et al.* Marine anoxia and delayed Earth system recovery after the end-Permian extinction. *Proc. Natl. Acad. Sci. U.S.A.* **113**, 2360–2365 (2016).

12. Korte, C. & Kozur, H. W. Carbon-isotope stratigraphy across the PermianTriassic boundary: A review. *Journal of Asian Earth Sciences* **39**, 215–235 (2010).

13. Erwin, D. H. *Extinction: How Life on Earth Nearly Ended 250 Million Years Ago-Updated Edition*, vol. 37 (Princeton University Press, 2015).

14. Penn, J. L., Deutsch, C., Payne, J. L. & Sperling, E. A. Temperature-dependent hypoxia explains biogeography and severity of end-Permian marine mass extinction. *Science* **362**, eaat1327 (2018).

15. Winguth, A. M. E. & Maier-Reimer, E. Causes of the marine productivity and oxygen changes associated with the PermianTriassic boundary: A reevaluation with ocean general circulation models. *Marine Geology* **217**, 283–304 (2005).

16. Winguth, C. & Winguth, A. M. E. Simulating PermianTriassic oceanic anoxia distribution: Implications for species extinction and recovery. *Geology* **40**, 127–130 (2012).

17. Meyer, K. M., Kump, L. R. & Ridgwell, A. Biogeochemical controls on photic-zone euxinia during the end-Permian mass extinction. *Geology* **36**, 747–750 (2008).

18. Meyer, K. M., Ridgwell, A. & Payne, J. L. The influence of the biological pump on ocean chemistry: implications for long-term trends in marine redox chemistry, the global carbon cycle, and marine animal ecosystems. *Geobiology* **14**, 207–219 (2016).

19. Zhang, F. *et al.* Multiple episodes of extensive marine anoxia linked to global warming and continental weathering following the latest Permian mass extinction. *Science Advances* **4**, e1602921 (2018).

20. Rothman, D. H. *et al.* Methanogenic burst in the end-Permian carbon cycle. *Proc. Natl. Acad. Sci. U.S.A.* **111**, 5462–5467 (2014).

21. Cui, Y., Kump, L. R. & Ridgwell, A. Initial assessment of the carbon emission rate and climatic consequences during the end-Permian mass extinction. *Palaeogeography, Palaeoclimatology, Palaeoecology* **389**, 128–136 (2013).

22. Clarkson, M. O. *et al.* Ocean acidification and the Permo-Triassic mass extinction. *Science* **348**, 229–232 (2015).

23. Meyer, K. M., Yu, M., Jost, A. B., Kelley, B. M. & Payne, J. L. δ13C evidence that high primary productivity delayed recovery from end-Permian mass extinction. *Earth and Planetary Science Letters* **302**, 378–384 (2011).

24. Song, H. *et al.* Large vertical δ13cdic gradients in Early Triassic seas of the South China craton: Implications for oceanographic changes related to Siberian Traps volcanism. *Global and Planetary Change* **105**, 7–20 (2013).

25. Luo, G. *et al.* Vertical 13Corg gradients record changes in planktonic microbial community composition during the end-Permian mass extinction. *Palaeogeography, Palaeoclimatology, Palaeoecology* **396**, 119–131 (2014).

26. Algeo, T. J. *et al.* Changes in productivity and redox conditions in the Panthalassic Ocean during the latest Permian. *Geology* **38**, 187–190 (2010).

27. Schobben, M. *et al.* Flourishing ocean drives the end-Permian marine mass extinction. *Proc. Natl. Acad. Sci. U.S.A.* **112**, 10298–10303 (2015). Publisher: National Academy of Sciences Section: Physical Sciences.

28. Boscolo-Galazzo, F. *et al.* Temperature controls carbon cycling and biological evolution in the ocean twilight zone. *Science* **371**, 1148–1152 (2021).

29. Kump, L. R., Pavlov, A. & Arthur, M. A. Massive release of hydrogen sulfide to the surface ocean and atmosphere during intervals of oceanic anoxia. *Geology* **33**, 397–400 (2005).

30. Keeling, R. F., Körtzinger, A. & Gruber, N. Ocean Deoxygenation in a Warming World. *Annual Review of Marine Science* **2**, 199–229 (2010).

31. Lu, W. *et al.* Late inception of a resiliently oxygenated upper ocean. *Science* **361**, 174–177 (2018).

32. López-Urrutia, A., Martin, E. S., Harris, R. P. & Irigoien, X. Scaling the metabolic balance of the oceans. *Proc. Natl. Acad. Sci. U.S.A.* **103**, 8739–8744 (2006).

33. Ridgwell, A. *et al.* Marine geochemical data assimilation in an efficient Earth System Model of global biogeochemical cycling. *Biogeosciences* **4**, 87–104 (2007).

34. Hülse, D., Arndt, S., Daines, S., Regnier, P. & Ridgwell, A. OMEN-SED 1.0: a novel, numerically efficient organic matter sediment diagenesis module for coupling to Earth system models. *Geoscientific Model Development* **11**, 2649–2689 (2018).

35. Hülse, D., Arndt, S., Wilson, J. D., Munhoven, G. & Ridgwell, A. Understanding the causes and consequences of past marine carbon cycling variability through models. *Earth-Science Reviews* **171**, 349–382 (2017).

36. Heim, N. A., Knope, M. L., Schaal, E. K., Wang, S. C. & Payne, J. L. Copes rule in the evolution of marine animals. *Science* **347**, 867–870 (2015).

37. Sinninghe Damsté, J. S., Kok, M. D., Köster, J. & Schouten, S. Sulfurized carbohydrates: an important sedimentary sink for organic carbon? *Earth and Planetary Science Letters* **164**, 7–13 (1998).

38. Walker, J. C. G., Hays, P. B. & Kasting, J. F. A negative feedback mechanism for the long-term stabilization of Earth's surface temperature. *Journal of Geophysical Research: Oceans* **86**, 9776–9782 (1981).

39. Van Cappellen, P. & Ingall, E. D. Benthic phosphorus regeneration, net primary production, and ocean anoxia: A model of the coupled marine biogeochemical cycles of carbon and phosphorus. *Paleoceanography* **9**, 677–692 (1994).

40. Schobben, M. *et al.* A nutrient control on marine anoxia during the end-Permian mass extinction. *Nature Geoscience* 1–7 (2020).

41. Hülse, D., Arndt, S. & Ridgwell, A. Mitigation of Extreme Ocean Anoxic Event Conditions by Organic Matter Sulfurization. *Paleoceanography and Paleoclimatology* **34**, 476–489 (2019).

42. Li, X. *et al.* Particulate sulfur species in the water column of the Cariaco Basin. *Geochimica et Cosmochimica Acta* **75**, 148–163 (2011).

43. Helly, J. J. & Levin, L. A. Global distribution of naturally occurring marine hypoxia on continental margins. *Deep Sea Research Part I: Oceanographic Research Papers* **51**, 1159–1168 (2004).

44. Montenegro, A. *et al.* Climate simulations of the Permian-Triassic boundary: Ocean acidification and the extinction event. *Paleoceanography* **26** (2011).

45. Naafs, B. D. A. *et al.* Fundamentally different global marine nitrogen cycling in response to severe ocean deoxygenation. *Proceedings of the National Academy of Sciences* **116**, 24979–24984 (2019).

46. Berner, R. A. The carbon and sulfur cycles and atmospheric oxygen from middle Permian to middle Triassic. *Geochimica et Cosmochimica Acta* **69**, 3211–3217 (2005).

47. Payne, J. L. & Kump, L. R. Evidence for recurrent Early Triassic massive volcanism from quantitative interpretation of carbon isotope fluctuations. *Earth and Planetary Science Letters* **256**, 264–277 (2007).

48. Ridgwell, A. A Mid Mesozoic Revolution in the regulation of ocean chemistry. *Marine Geology* **217**, 339–357 (2005).

49. Elrick, M. *et al.* Global-ocean redox variation during the middle-late Permian through Early Triassic based on uranium isotope and Th/U trends of marine carbonates. *Geology* **45**, 163–166 (2017).

50. Zhang, F. *et al.* Congruent Permian-Triassic δ238u records at Panthalassic and Tethyan sites: Confirmation of global-oceanic anoxia and validation of the U-isotope paleoredox proxy. *Geology* **46**, 327–330 (2018).

51. Zhang, F. *et al.* Global-ocean redox variations across the Smithian-Spathian boundary linked to concurrent climatic and biotic changes. *Earth-Science Reviews* **195**, 147–168 (2019).

52. Schobben, M., Joachimski, M. M., Korn, D., Leda, L. & Korte, C. Palaeotethys seawater temperature rise and an intensified hydrological cycle following the end-Permian mass extinction. *Gondwana Research* **26**, 675–683 (2014).

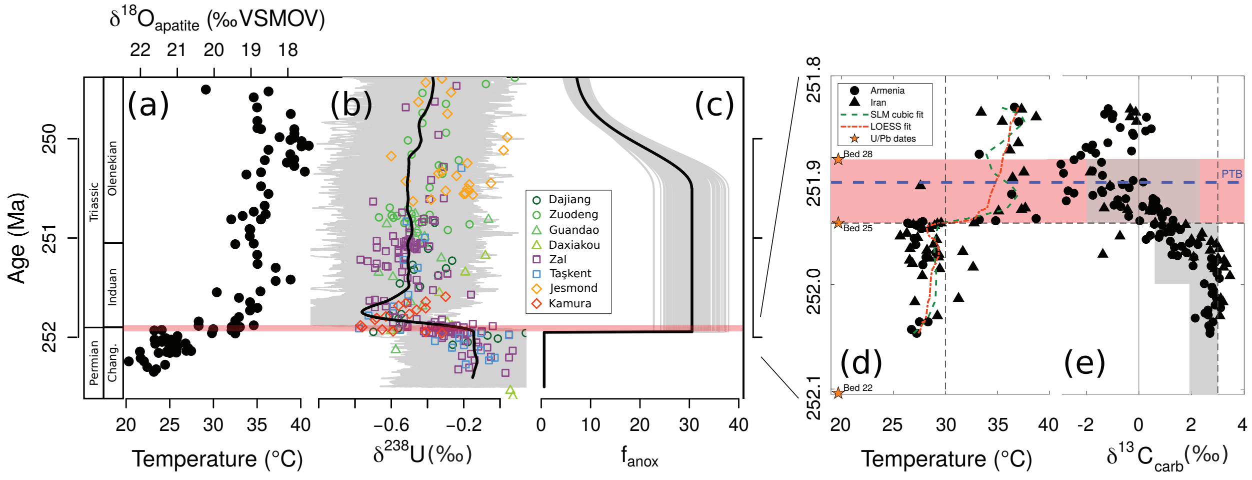

Figure 1: **Temporal relationship of changes in isotope records and U mass balance modeling for the P/Tr extinction.** (a) Temperature reconstructions from the δ^{18}O of biogenic apatite from South China (black circles)[6]. (b) Carbonate δ^{238}U data (colored symbols)[11,19,49–51]. U isotope forward model results are shown, with gray lines representing individual iterations from the Monte Carlo routine with variable isotopic fractionation into anoxic sediments, riverine δ^{238}U, and carbonate diagenetic offset. The black line represents the moving average of all model runs (SI). (c) Varying perturbations in seafloor anoxic fraction (f_{anox}) that drive the U-model in panel b (individual iterations, grey lines; average, black line). (d + e) Conodont apatite δ^{18}O and δ^{13}C[8,52] (SI). Grey shading in (e) represents the range of cGENIE δ^{13}C values simulated for the Tethys Ocean for the experiments shown in Fig. 3.

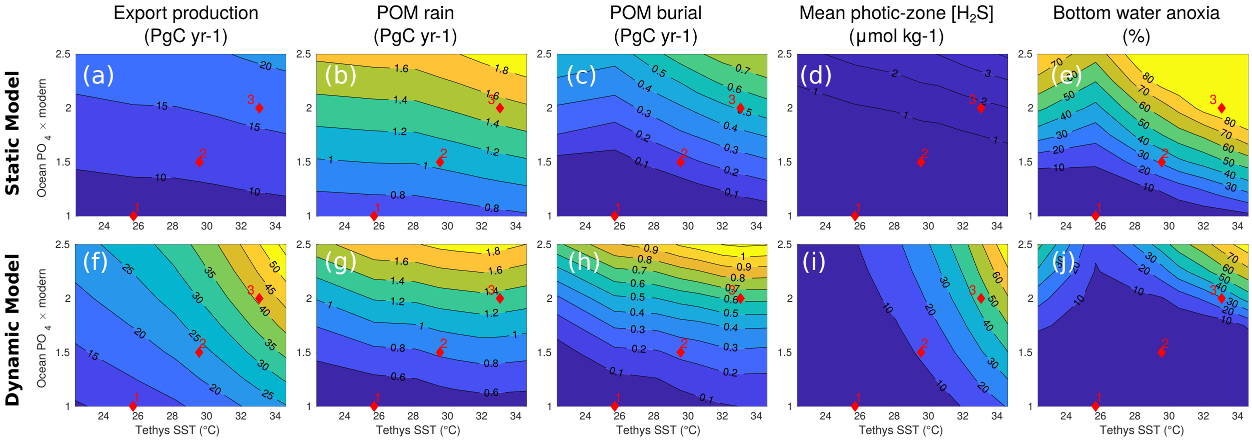

Figure 2: **Global sensitivity of particulate organic matter (POM) cycling and ocean redox to temperature and phosphate changes** for the static and dynamic representation of the biological pump: POM flux values (in PgC yr^{-1}) of export production (a+f), POM rain to the seafloor (b+g) and POM burial in the sediments (c+h). Mean photic-zone $[H_2S]$ (in μmol kg^{-1}, d+i) and bottom water anoxia (e+j) as fraction of seafloor area with $[O_2] \leq 5\mu$mol kg^{-1} (in %). The red diamonds indicate results for the experiments presented in Fig. 3.

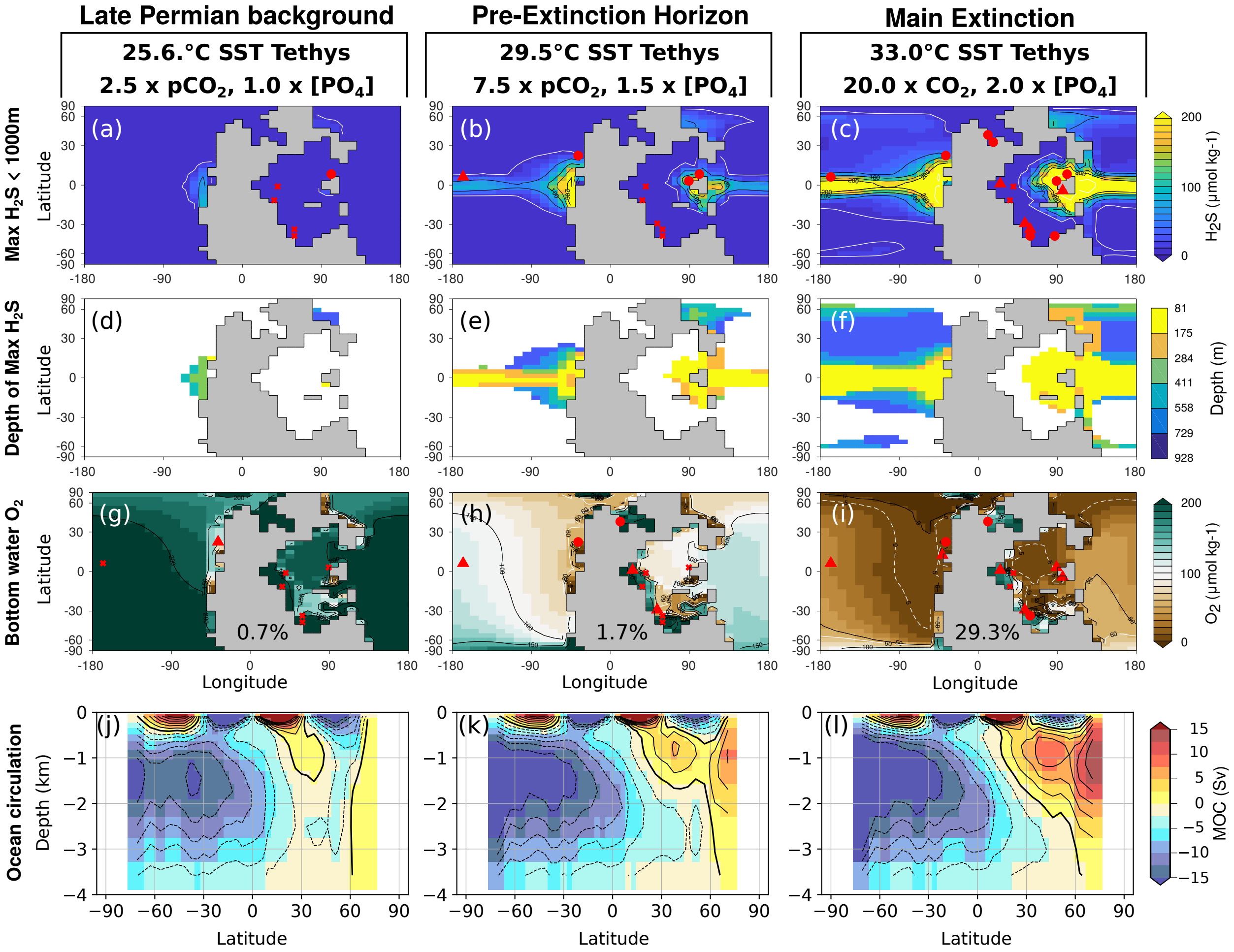

Figure 3: **Ocean redox conditions during the P/Tr transition using the dynamic cGENIE model:** (a-c): Simulated maximum [H_2S] between 81 and 928m. (d-f): Depth where the maximum in [H_2S] is observed. (g-i): Simulated extent of seafloor anoxia (values indicate f_{anox}). Model results for [H_2S] and [O_2] are superimposed by proxy observations: Evidence for euxinia/anoxia is represented by circles; evidence against by crosses; ambiguous evidence or dynamic redox-conditions by triangles (see Extended Data Table 2). (j-l): Meriodional overturing circulation (MOC, in Sv).

Acknowledgements We gratefully acknowledge data contributions from M. Joachimski and advice on how to align proxy-records. We would like to thank M. Schobben, Y. Sun and an anonymous reviewer for their contructive comments. D.H. is supported by a postdoctoral fellowship from the Simons Foundation (Award 653829). S.J.V. is a NASA Postdoctoral Program fellow. D.H. and A.R. acknowledge support from the Heising-Simons Foundation.

Author contributions D.H., K.V.L. and A.R. conceived the study; D.H. and A.R. designed and conducted cGENIE experiments; K.V.L. adapted the U-model and conducted the experiments; K.V.L. and D.H. compiled and analyzed the proxy-data; All authors analyzed model output. D.H., K.V.L. and A.R. wrote the manuscript with input from all authors.

Competing Interests The authors declare no competing interests.

Supplementary Information is available for this paper.

Correspondence and requests for materials should be addressed to D.H. (email: dominik.huelse@ucr.edu).

Data availability

The locations of all data used in this study are provided in the supplementary information.

Code availability

The version of the code used in this paper is tagged as release v0.9.15 and has a DOI of 10.5281/zenodo.4008865. Necessary boundary condition files are included as part of the code release. Configuration files for the specific experiments presented in the paper can be found in the installation subdirectory: genie-userconfigs/MS/huelseetal.2020. Details of the experiments, plus the command line needed to run each one, are given in the readme.txt file in that directory. A manual describing code installation, basic model configuration, and an extensive series of tutorials is provided. The Latex source of the manual and pre-built PDF file can be obtained by cloning (https://github.com/derpycode/muffindoc).